Article

Promoting the OH cycle on an activated dynamic interface for electrocatalytic ammonia synthesis

Jiabao Lv[1,2], Ang Cao[1,3], Yunhao Zhong[1], Qingyang Lin[1], Xiaodong Li[1], Hao Bin Wu[4] ✉, Jianhua Yan[1] ✉ & Angjian Wu[1,2] ✉

Renewable-driven electrocatalytic nitrate conversion offers a promising alternative to alleviate nitrate pollution and simultaneously harvest green ammonia. However, due to the complex proton-electron transfer processes, the reaction mechanism remains elusive, thereby limiting energy efficiency. Here, we adopt $Ni(OH)_2$ as a model catalyst to investigate the dynamic evolution of the reaction interface. A proposed OH cycle mechanism involves the formation of a locally OH-enriched microenvironment to promote the hydrogenation process, which is identified through in-situ spectroscopy and isotopic labelling. By further activating the dynamic state through the implementation of surface vacancies via plasma, we achieve a high Faradaic efficiency of almost 100%. The activated interface accelerates the OH cycle by enhancing dehydroxylation, water dissociation, and OH adsorption, thereby promoting nitrate electroreduction and inhibiting hydrogen evolution. We anticipate that rational activation of the dynamic interfacial state can facilitate electrocatalytic interface activity and improve reaction efficiency.

Ammonia (NH_3), a vital platform compound for agriculture and industry with a global demand exceeding 150 million tons annually[1,2], accounts for 1–2% of the world's energy supply and superabundant CO_2 emission[3,4]. Large-scale NH_3 production is currently dominated by the fossil-fuel-driven Haber-Bosch process, operating under harsh conditions (approximately 400–500 °C and 150–350 atm)[5-7]. As an alternative, the direct electrocatalytic nitrate reduction reaction (NO_3RR) powered by renewable electricity, provides decentralized and sustainable NH_3 production at ambient conditions[8-12]. Compared to the inert and low soluble N_2 molecules (N≡N bond, 948 kJ/mol), nitrate promises lower dissociation energy (N=O bond, 204 kJ/mol) with improved reaction kinetics[13,14]. Furthermore, nitrate is widely distributed in industrial wastewater and contaminated groundwater, its conversion through the denitrification process is essential for restoring the global nitrogen cycle imbalance. Therefore, developing electrocatalytic NO_3RR can enable a promising route for green NH_3

production and simultaneously mitigate environmental burdens, aiming at the transition towards carbon-neutral society[15,16].

Despite significant advancements in catalyst design for NO_3RR, achieving ampere-level current density and nearly unit Faradaic efficiency (FE), the fundamental understanding of the intrinsic active sites and reaction process remains ambiguous[17-19]. The transition metals (such as Ni, Co, and Cu)-based electrocatalysts previously claimed promising NO_3RR activity, commonly suffer dynamic phase change or surface reconstruction as exposure to electrolytes and reactants at operating potential, which makes it challenging to explore the underlying mechanism[20,21]. Recent studies anticipated the fluctuating reactive interface might facilitate the catalytic conversion rather than the initial well-defined static catalytic center or pristine state[22]. As for NO_3RR involved with the multi-step proton-electron transfer, various intermediate species might be formed accompanied with the change of interface state, ultimately affecting the possible reaction pathways

[1]State Key Laboratory of Clean Energy Utilization, Zhejiang University, Hangzhou, P. R. China. [2]Baima Lake Laboratory, Hangzhou, P. R. China. [3]Department of Physics, Technical University of Denmark, Kongens Lyngby, Denmark. [4]State Key Laboratory of Silicon Materials, School of Materials Science and Engineering, Zhejiang University, Hangzhou, P. R. China. ✉e-mail: hbwu@zju.edu.cn; yanjh@zju.edu.cn; wuaj@zju.edu.cn
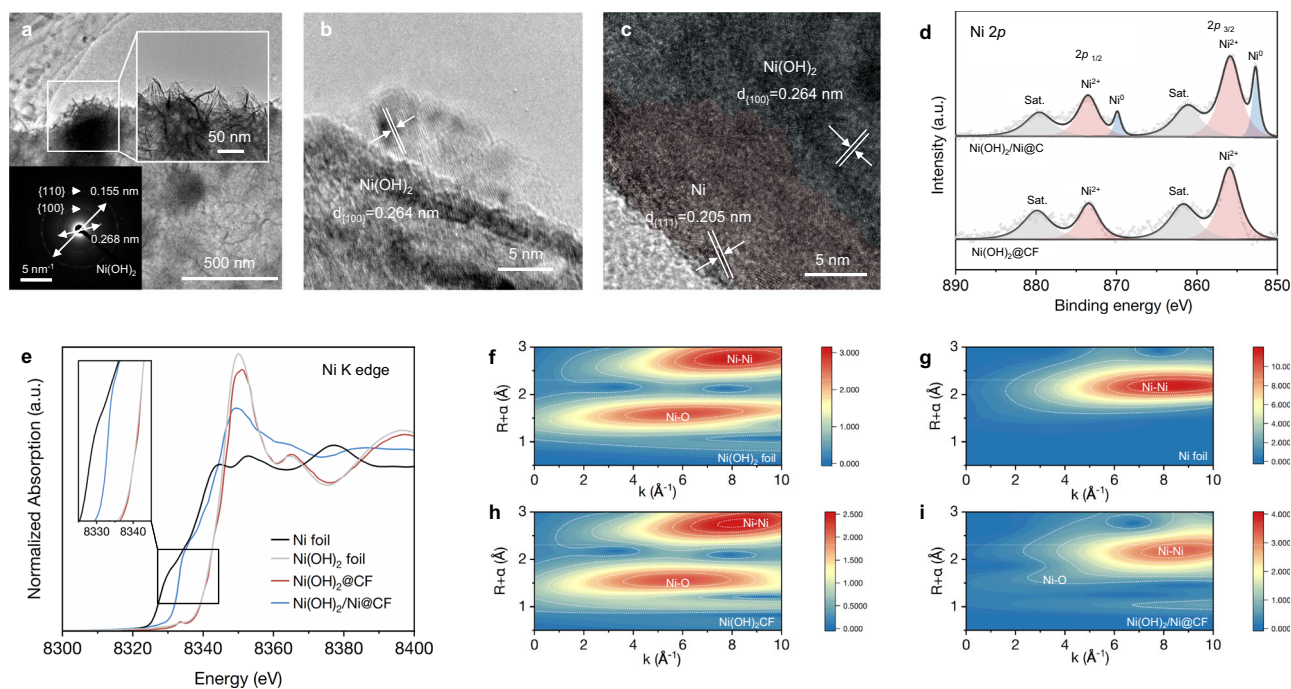
Fig. 1 | Characterization of the Ni(OH)₂@CF and Ni(OH)₂/Ni@CF. a TEM image and SAED pattern of Ni(OH)₂@CF (scale bar: 500 nm). HR-TEM images of (**b**) Ni(OH)₂@CF and (**c**) Ni(OH)₂/Ni@CF (scale bar: 5 nm). **d** Ni 2p XPS spectra of Ni(OH)₂/Ni@CF. **e** Ni K-edge XANES spectra of Ni(OH)₂@CF and Ni(OH)₂/Ni@CF (inset: Fourier transformed Ni K-edge EXAFS spectra corresponding to the XANES spectra). Wavelet transformation of (**f**) Ni(OH)₂ foil, (**g**) Ni foil (**h**) Ni(OH)₂@CF, and (**i**) Ni(OH)₂/Ni@CF. Source data for Fig. 1 are provided as a Source Data file.

(NH₃ or by-products like N₂, NO, N₂H₄, etc.,) and activity of NH₃ production[23]. Additionally, the dynamic evolution of the catalytic interface is determined by the synergistic effect of potential and microenvironment, thereby impacting the reaction performance[24]. The interplay between the evolved catalyst surface and interfacial electrolyte plays a crucial role in the water dissociation and subsequent protonation process for targeted NH₃ synthesis or competing hydrogen evolution reaction (HER), while rare studies have been further investigated. Hence, it is essential to identify the mechanism of the dynamic interface and elucidate its correlation to the key intermediates and reaction activity, by providing a strategy to manipulate and improve nitrate conversion.

Herein, we tracked the dynamic interface and investigated the NO₃RR mechanism using typical nickel hydroxide as model catalyst. In-situ characterization combined with theoretical calculation demonstrated the potential-induced change from Ni(OH)₂ to Ni(OH)₂/Ni. The free diffusion of OH species was assumed to be restricted at the metastable interface along with the generation of a local-OH-enrich region, which enhanced the hydrogenation of nitrogen species while inhibiting HER. Then, the interface was further activated by constructing rich vacancies using non-thermal plasma (NTP) modification. Operando Raman-FTIR-EPR and kinetic isotopic labeling revealed that the NTP-activated interface significantly accelerated the dynamic interaction between catalyst and electrolyte, to promote the potential kinetic of the OH cycle and proton transfer. As a result, a high NH₃ production activity was achievd with the FE of almost 100%, exhibiting the economic and environmental prospects of green NH₃ production.

Results

Characterization of the catalyst surface reconstruction

Lamellar structure Ni(OH)₂ with distinct transparent edges was facilely synthesized on Cu foam (CF) via electrodeposition to obtain Ni(OH)₂@CF, where CF was employed as the substrate and skeleton to ensure sufficient conductivity (Supplementary Figs. S1, S2). The uniform distribution of Ni, Cu and O elements across the Ni(OH)₂@CF

catalyst was observed by Energy-dispersive X-ray Spectroscopy (EDX) mapping (Supplementary Fig. S3). X-ray diffraction (XRD) pattern of prepared Ni(OH)₂@CF demonstrated the appearance of {100} and {110} crystalline planes corresponding to Ni(OH)₂ (Supplementary Fig. S4), consistent with the selected area electron diffraction (SAED) and the typical lattice spacing (0.264 nm) discerned in high-resolution transmission electron microscopy (HR-TEM) (Fig. 1a, b). Besides, the prepared catalyst was stripped and characterized independently via X-ray photoelectron spectroscopy (XPS) and inductively coupled plasma optical emission spectroscopy (ICP-OES), respectively, which confirmed the absence of Cu on the catalyst surface and excluded the potential influence of Cu on enhanced reaction activity (Supplementary Table. S1, Supplementary Fig. S5). During NO₃RR, the oxidized state (Ni²⁺) of Ni(OH)₂@CF proceeded reduction together with structural reconstruction at the top layers of the catalyst surface. Under the potential at −0.8 vs RHE, a lattice stripe of 0.205 nm belonging to Ni {111} facet emerged, suggesting the potential-dependent transition from Ni(OH)₂@CF to Ni(OH)₂/Ni@CF (Fig. 1c), corroborated by the XRD patterns (Supplementary Fig. S6). Additionally, the presence of a Ni⁰ peak at a binding energy of ~853 eV in Ni 2p spectra was also observed through XPS (Fig. 1d).

To obtain the precise atomic-scale understanding of the catalyst, the local structure and valence state of Ni(OH)₂/Ni@CF and Ni(OH)₂@CF were comparatively examined through Ni K-edge X-ray absorption spectroscopy (XAS) (Supplementary Figs. S7–8, Supplementary Table S2). Ni(OH)₂@CF exhibited similar peak characteristics to the Ni(OH)₂ foil in X-ray absorption near-edge structure (XANES) spectra (Fig. 1e), while Ni(OH)₂/Ni@CF displayed dominant metallic Ni-Ni bond in the extended X-ray absorption fine structure (EXAFS) R-space spectra (Supplementary Fig. S9). However, it was evident in XANES that the absorption edge of Ni(OH)₂/Ni@CF located at a higher energy region compared to Ni foil (Fig. 1e: inset). Additionally, the wavelet transform (WT) of EXAFS revealed that Ni(OH)₂/Ni@CF exhibited both the metallic Ni-Ni bond signal and the Ni-O signal (1 - 2 Å) (Fig. 1f–i). To precisely determine the Ni valence state, the
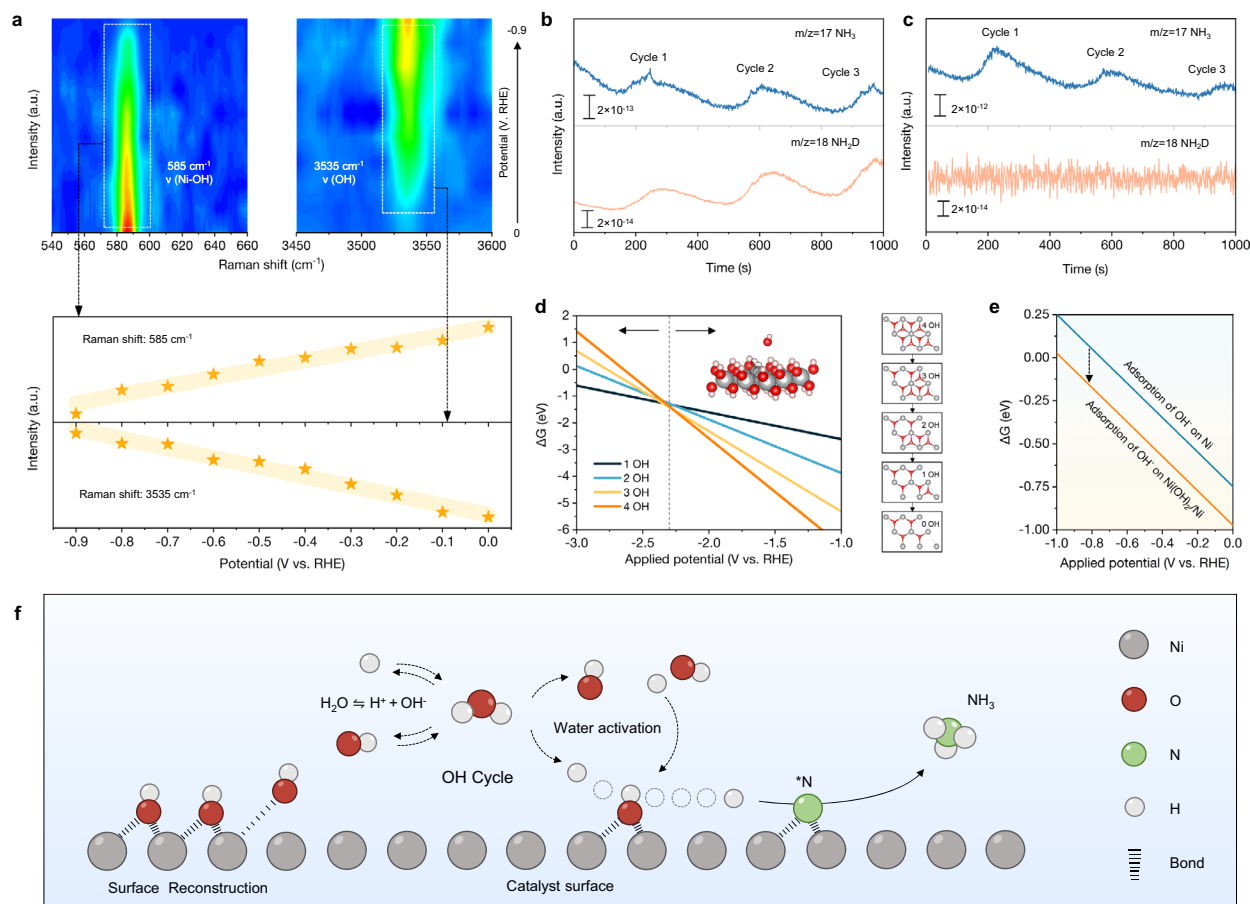
Fig. 2 | Mechanism study of the OH cycle. a In-situ electrochemical Raman spectra of Ni(OH)$_2$/Ni@CF from 0 to −0.9 V vs. RHE (without iR compensation) in the electrolyte with 0.1 M KNO$_3$ + 1 M KOH. Below: The intensity of the Raman signal at 585 cm^{-1} and 3535 cm^{-1} (scatter: real Raman signal; line: polynomial fitting curve). In-situ electrochemical DEMS result of the D/H isotope labelled catalyst pre-operated in (**b**) D$_2$O solvent and (**c**) H$_2$O solvent, respectively. **d** Calculated surface Pourbaix diagrams for Ni(OH)$_2$/Ni as the function of applied potential at pH = 14 (right: corresponding structure of different phases of Ni(OH)$_2$/Ni; Gray, red, and pink spheres represent Ni, O, and H atoms, respectively). **e** Absorption ability of OH on pure Ni and Ni(OH)$_2$ induced Ni(OH)$_2$/Ni surface, respectively. **f** Schematic diagram during NO$_3$RR process including OH cycle mechanism. Source data for Fig. 2 are provided as a Source Data file.

average oxidation states were fitted by taking the valence of Ni (0.00) and Ni(OH)$_2$ (2.00) at 0.4 of normalized absorption as standards from Ni K-edge XANES. The nominal valence state of Ni in Ni(OH)$_2$/Ni@CF (+ 0.35) was located between Ni(OH)$_2$ (+ 2.00) and Ni (0.00) (Supplementary Fig. S10). Overall, the XAS result confirmed that a significant amount of Ni^0 species was generated on the surface after electroreduction, while the mixed state of Ni(OH)$_2$/Ni was still retained.

Mechanism study of OH cycle on the dynamic interface

In-situ electrochemical Raman spectroscopy was employed to monitor the dynamic interface and evolved active sites during NO$_3$RR. The peak at 585 cm^{-1} corresponding to the Ni−OH stretching modes was observed and the broad spectra peak at 3535 cm^{-1} was assigned to the surface O−H stretching bands[25–27] (Fig. 2a, and Supplementary Fig. S11). As the potential negatively shifted from 0 to −0.9 V vs. RHE, Ni−OH intensity decreased, accompanied by the increase of surface O-H intensity simultaneously, which implied the intimate relationship between de-hydroxylation process and the presence of interfacial OH, occurring in the transition from initial Ni(OH)$_2$ to Ni(OH)$_2$/Ni during NO$_3$RR. In-situ differential electrochemical mass spectrometry (DEMS) measurements were further carried out using H/D isotopic labeling to understand the OH evolution process. Firstly, the catalyst was labeled by operating in the electrolyte with H$_2$O and D$_2$O solvent, respectively. Then, NO$_3$RR was performed in the electrolyte with H$_2$O solvent after

thoroughly washing, and the generated volatile products were measured using DEMS (Supplementary Figs. S12–13)[28]. As predicted, NH$_x$D$_{3-x}$ signals (m/z = 18, 19, and 20) assigned to NH$_2$D, NHD$_2$, and ND$_3$ was only detected on the catalyst pretreated in D$_2$O solvent, providing solid evidence that the lattice OH interchanged with the electrolyte OD and thus participated in hydrogenation process during reaction (Fig. 2b, c)[29].

To further elucidate the role of OH migration as well as the interplay between catalyst surface and electrolyte during NO$_3$RR, serial isotopic labelling experiments were designed to trace the dynamic interface behaviour using attenuated total reflection Fourier transformed infrared (ATR-FTIR) spectroscopy (Supplementary Fig. S14). (I) Initially, the Ni(OD)$_2$@CF catalyst prepared via D$_2$O was employed for NO$_3$RR with H$_2$O-based electrolyte. The peak located at 2497.7 cm^{-1} and 3343.6 cm^{-1} was discerned, assigning to D$_2$O and H$_2$O species, respectively (Supplementary Fig. S15). The semi-quantitative ratio of D$_2$O/H$_2$O (D/H) determined by FTIR was 0.26, consistent with the result of Raman spectra (Supplementary Figs. S16–17). The appearance of D$_2$O species implied that the interfacial OH from the catalyst participated in NO$_3$RR with water as a medium via the equilibrium of water dissociation. (II) After 30 mins of operation, we refreshed the electrolyte and continued NO$_3$RR, while almost no D$_2$O was detected, implying the depletion of D-containing hydroxyl group on previous catalyst surface. (III) Subsequently, the catalyst was soaked in D$_2$O at open circuit potential (OCP) and was tested again, with the D/H ratio of
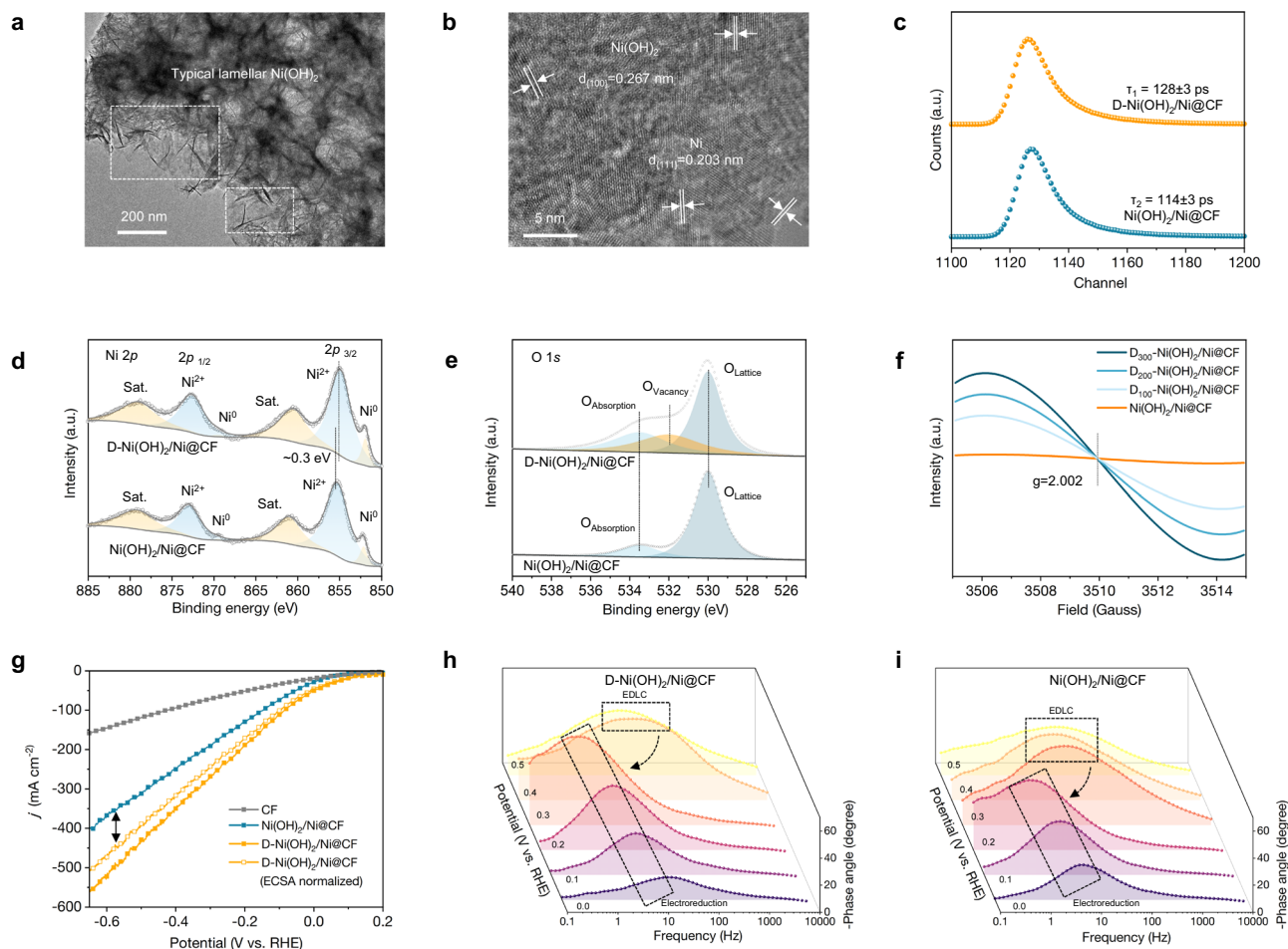
Fig. 3 | Structural analysis and electrochemical diagnosis of D-Ni(OH)$_2$/Ni@CF.
a HR-TEM image of D-Ni(OH)/Ni@CF with scale bar of 200 nm. **b** HR-TEM image of
D-Ni(OH)/Ni@CF with scale bar of 5 nm. **c** PALS spectra of Ni(OH)$_2$/Ni@CF and D-
Ni(OH)$_2$/Ni@CF. **d** Ni 2p XPS spectra of Ni(OH)/Ni@CF and D-Ni(OH)/Ni@CF. **e** O
1s XPS spectra of Ni(OH)/Ni@CF and D-Ni(OH)/Ni@CF. **f** EPR spectra of D-Ni(OH)/
Ni@CF with different plasma input power (100 ~ 300 W). **g** Polarization curves
measured by linear sweep voltammetry (LSV) from 0.2 to -0.65 V vs. RHE (without

iR compensation, resistance between RE and WE: 1.6 Ω, 5 mV s^{-1}) of CF, Ni(OH)$_2$/
Ni@CF, D-Ni(OH)$_2$/Ni@CF, and ECSA normalized D-Ni(OH)$_2$/Ni@CF, respectively
(j ECSA normalized D-Ni(OH)2/Ni@CF =j D-Ni(OH)2/Ni@CF * ECSA Ni(OH)2/Ni@CF / ECSA D-Ni(OH)2/
Ni@CF). Operando EIS plots from 0.5 to 0 V vs. RHE (without iR compensation) of (**h**)
D-Ni(OH)$_2$/Ni@CF and (**i**) Ni(OH)$_2$/Ni@CF with a frequency range from 0.1 Hz to
10 kHz (EDLC: electrochemical double-layer capacitor). Source data for Fig. 3 are
provided as a Source Data file.

the electrolyte increased to 0.17. This phenomenon demonstrated that
the Ni(OD)$_2$/Ni interface was not static, where the metallic Ni readily
regenerated into Ni(OD)$_2$ in solvent. (V-VI) The process was repeated
to ensure accuracy and reproducibility. Thus, we inferred that the joint
effect of spontaneous adsorption of OH and potential-dependent de-
hydroxylation caused a dynamic interface of Ni(OH)$_2$/Ni during
NO$_3$RR, which might induce the local OH species enriched region at the
electrode-electrolyte interface.

Density functional theory (DFT) calculation was performed to get
insight into the mechanism theoretically. Firstly, the actual state of the
catalyst surface under electrocatalysis conditions was determined by
establishing Pourbaix diagrams (Fig. 2d). A Ni(OH)$_2$ surface with a
supercell size of 2× 2 was selected as the calculation model. By nega-
tively shifting the potential to the Ni(OH)$_2$ surface, a phase transition
occurred, resulting in the de-hydroxylation of the surface and the
exposure of the metallic Ni phase, which is thermodynamically
favourable. Consistently, the energy barrier of the potential-
determined step (PDS) on Ni(OH)$_2$/Ni (0.48 eV) was lower than that
of Ni(OH)$_2$ (1.40 eV) (Supplementary Figs. S18–20, Supplementary
Table S3), and the crystal orbital Hamilton population (COHP) proved
the better adsorption capacity for NO$_3^-$ on Ni(OH)$_2$/Ni (Supplementary
Fig. S21), revealing the genuine active site originated from Ni(OH)$_2$/Ni

surface. Furthermore, we compared the ability of the OH capture on Ni
site between pure metal Ni (−0.75 eV) and Ni(OH)$_2$/Ni surface
(−0.97 eV), implying a better absorption of OH to form local enrich-
ment on Ni(OH)$_2$/Ni surface (Supplementary Fig. S22, Fig. 2e). Fur-
thermore, the dynamic adsorbed OH on exposed Ni could efficiently
activate interfacial H$_2$O dissociation and promote proton transfer[30].
Overall, the experiment and calculation revealed that the dynamic
process of surface OH desorption → limited OH diffusion → OH parti-
cipation in the hydrogenation constituted the surface OH cycle and in-
situ construction of active Ni(OH)$_2$/Ni interface, driving the efficient
nitrate-to-NH$_3$ conversion (Fig. 2f).

Design of the activated catalyst to promote OH cycle
To further activate the dynamic interface, we employed NTP to syn-
thesize defects-rich D-Ni(OH)$_2$@CF with more exposed OH vacancies,
aiming at enhancing surface OH cycle effect (Fig. S23). As expected,
HR-TEM images of D-Ni(OH)$_2$/Ni@CF showed the co-existence of lat-
tice fringe of 0.267 nm and 0.203 nm, corresponding to the {100} facet
of Ni(OH)$_2$ and {111} facet of Ni after NO$_3$RR, consistent with the XRD
pattern (Fig. 3a, b, Supplementary Fig. S24). Positron annihilation
lifetime spectroscopy (PALS) manifested the extension of the defect
relaxation time τ_1 from 114 to 128 ps, providing intuitionally evidence
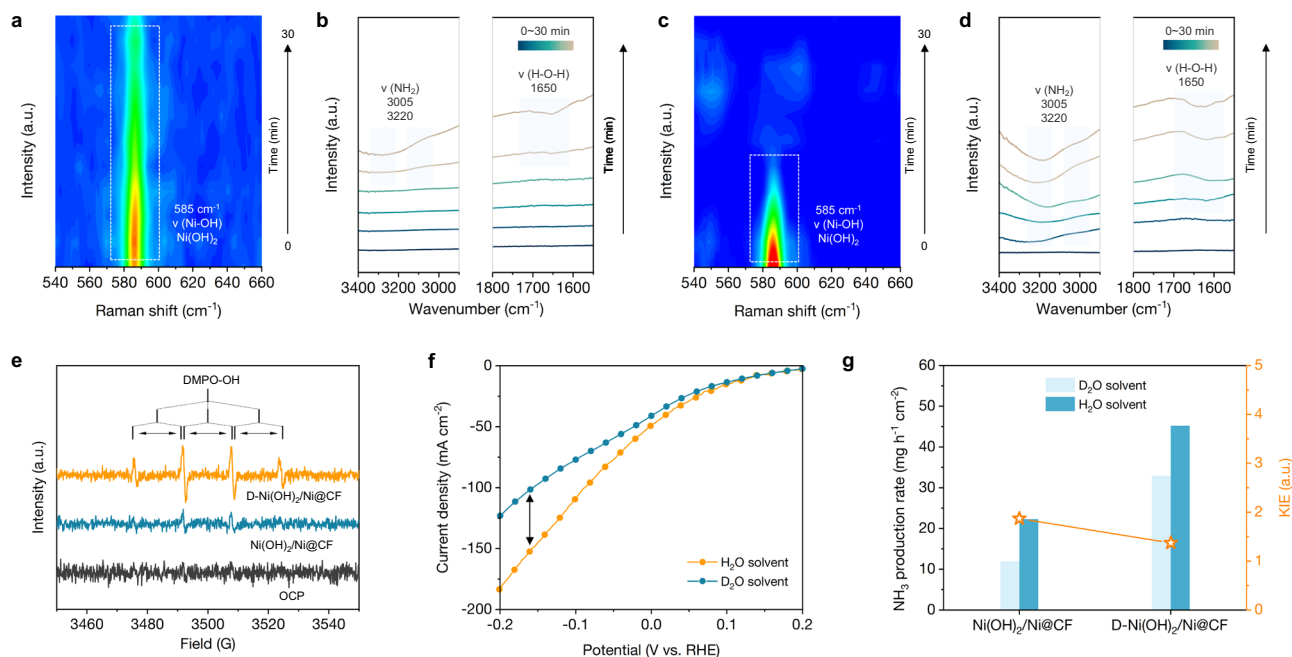
Fig. 4 | Study on the origin of OH cycle-enhanced catalytic activity. In-situ electrochemical Raman spectra at −0.8 V vs. RHE (without iR compensation) of (**a**) Ni(OH)$_2$/Ni@CF and (**c**) D-Ni(OH)$_2$/Ni@CF with a time scale of 0 - 30 min. In-situ electrochemical FTIR spectra at −0.8 V vs. RHE (without iR compensation) of (**b**) Ni(OH)$_2$/Ni@CF and (**d**) D-Ni(OH)$_2$/Ni@CF with a time scale of 0 - 30 min. **e** Quasi in-situ EPR spectra of collected electrolyte from NO$_3$RR using D-Ni(OH)$_2$/Ni@CF

and Ni(OH)$_2$/Ni@CF as electrocatalysts at −0.8 V vs. RHE (without iR compensation) in 1 M KOH with 0.1 M KNO$_3$. **f** Polarization curves (without iR compensation, 5 mV s^{-1}) of D-Ni(OH)$_2$/Ni@CF in H$_2$O and D$_2$O solutions. **g** H/D kinetic isotope effect during NO$_3$RR on different catalysts in 1 M KOH + 0.1 M KNO$_3$ using H$_2$O and D$_2$O as solvent at −0.8 V vs. RHE (without iR compensation). Source data for Fig. 4 are provided as a Source Data file.

for the increased defect dimensions on D-Ni(OH)$_2$/Ni@CF (Fig. 3c, and Supplementary Table S4). Compared to Ni(OH)/Ni@CF, the Ni 2$p_{3/2}$ peak on D-Ni(OH)$_2$/Ni@CF (854.8 eV) shifted ~0.3 eV to the lower binding energy level (Fig. 3d), along with a new peak emerged at 531.8 eV emerged in O 1s XPS spectra prominently, indicating the presence of OH vacancies on the surface (Fig. 3e)[31,32]. The constant presence of OH vacancies signals on the catalyst surface after the reaction suggested the stable existence of the defect. Quantified by the electron paramagnetic resonance (EPR)[33], the defect concentration of D-Ni(OH)$_2$/Ni@CF was intimately related to the energy density of applied NTP, with an approximately monotonic increased peak intensity with the plasma power from 100 to 300 W (Fig. 3f). Correspondingly, the ratio of Ni^0:Ni^{2+} increased from 0.01 to 0.06, with the monotonic shift of the Ni 2p peak position from 0.15 to 0.32 eV, indicating the reducing of surface Ni-OH species via NTP treatment (Supplementary Figs. S25–27)[34,35].

To clarify the electrochemical activity of D-Ni(OH)$_2$/Ni@CF, a typical three-electrode system using H-type cell was applied. We initially evaluated the ESCA of the freshly prepared catalyst for comparison, revealing the comparable C$_{dl}$ values for D-Ni(OH)$_2$/Ni@CF (57.3 mF cm^{-2}) and Ni(OH)$_2$/Ni@CF (51.9 mF cm^{-2}) (Supplementary Figs. S28–29). Polarization curves exhibited a substantially lower overpotential and larger current density of D-Ni(OH)$_2$/Ni@CF (−562.6 mA cm^{-2}) compared to CF (157.63 mA cm^{-2}) and Ni(OH)$_2$/Ni (400.45 mA cm^{-2}), indicating accelerated kinetics of NO$_3$RR electrochemical reaction on activated interface (Fig. 3g). After normalizing the current density of D-Ni(OH)$_2$/Ni@CF to that of Ni(OH)$_2$/Ni@CF by ECSA, the catalytic activity remained superior (503.96 mA cm^{-2}), excluding the effect from the surface roughness modification by NTP. Additionally, D-Ni(OH)$_2$/Ni also showed better catalytic activity in the electrolyte without nitrate, implying its capability to reduce overpotential and promote proton transfer by optimizing OH adsorption and water dissociation (Supplementary Fig. S30). Similarly, the results of electrochemical impedance spectroscopy (EIS) further supported

the lowest charge transfer resistance on D-Ni(OH)$_2$/Ni@CF of 0.97 Ω (4.22 Ω of CF and 1.24 Ω of Ni(OH)$_2$/Ni@CF, respectively) (Supplementary Figs. S31–32). Through long-term electrosynthesis of NH$_3$, the ECSA on D-Ni(OH)$_2$/Ni@CF (105.05 mF cm^{-2}) increased more significantly than that of Ni(OH)$_2$/Ni@CF (64.20 mF cm^{-2}), reflected the faster surface evolution on the activated dynamic interface with more active sites (Supplementary Figs. S33–34). To analyze the electrochemical dynamics of the catalyst surface, Operando EIS was performed during NO$_3$RR (Fig. 3h–i). The peaks in the high-frequency region corresponded to the charging process of the electrochemical double-layer capacitor (EDLC), while the peaks in the low-frequency region were associated with the electroreduction process[36]. It was observed that a notable transition from the EDLC behavior to electroreduction behavior at +0.3 V vs. RHE over D-Ni(OH)$_2$/Ni@CF, higher than that over Ni(OH)$_2$/Ni@CF (+ 0.2 V vs. RHE), which implied the lower onset potential and better catalytic performance of D-Ni(OH)$_2$/Ni@CF.

Kinetic study of the promoted OH cycle

To elucidate the impact of the activated interface of D-Ni(OH)$_2$/Ni@CF on OH cycle, we performed the temporal-scale analysis via in-situ Raman/FTIR spectroscopy. The Ni(OH)$_2$ signal gradually attenuated but still maintained on Ni(OH)$_2$/Ni@CF from 0 to 30 mins in Raman spectra (Fig. 4a, Supplementary Fig. S35). In contrast, D-Ni(OH)$_2$/Ni@CF experienced rapid deterioration and completely obliterated, implying the acceleration of de-hydroxylation effect over the catalyst surface after NTP treatment (Fig. 4c). In-situ FTIR measurements were also conducted, and the peaks at 3005 and 3220 cm^{-1} were attributed to N species[24,37], and the peaks at ~1650 cm^{-1} were attributed to OH group[38]. According to FTIR spectroscopy, notable peak signals corresponding to active N species (e.g. *NH$_2$) and interface water were observed at the onset of the reaction on D-Ni(OH)$_2$/Ni@CF and gradually strengthened with the reaction. The rapid adsorption of N species and the surface de-hydroxylation based on in-situ FTIR/Raman
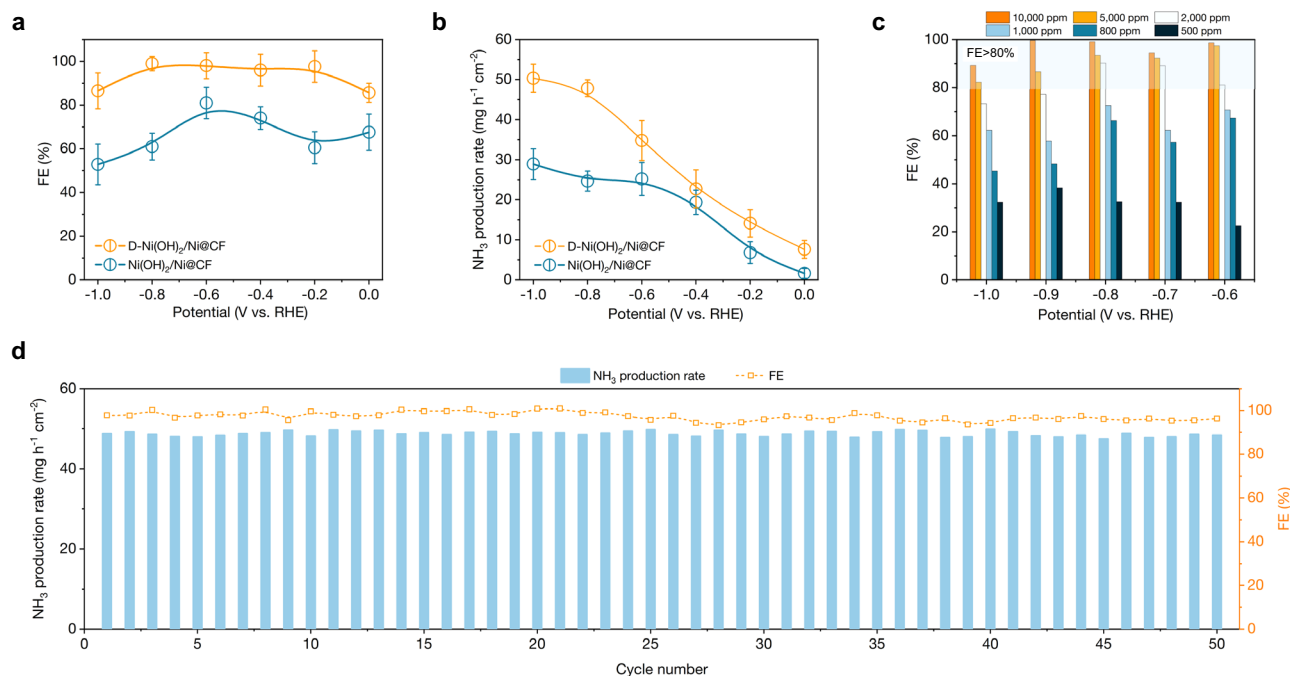
Fig. 5 | Electrocatalytic NO₃RR performance. a FE and (**b**) NH₃ production rate on Ni(OH)₂/Ni@CF and D-Ni(OH)₂/Ni@CF in 1 M KOH + 0.1 M KNO₃ electrolyte at the potential range from 0.0 V vs. RHE to −1.0 V vs. RHE (without iR compensation, the resistance between RE and WE: 1.6 Ω) (error bars: standard deviations of 3 independent measurements, center value: average of the 3 independent measurements). **c** FE from −0.6 to −1.0 V vs. RHE (without iR compensation) in 1 M KOH with different NO₃⁻ concentrations from 500 to 10,000 ppm. (**d**) NH₃ production rate and FE at −0.8 V vs. RHE in 1 M KOH + 0.1 M KNO₃ (without iR compensation) of D-Ni(OH)₂/Ni@CF for 50 cycle numbers (one hour per cycle). Source data for Fig. 5 are provided as a Source Data file.

imply the faster reconstruction and reaction kinetics over D-Ni(OH)₂/Ni@CF to promote water dynamics and proton transfer (Fig. 4b, d).

To quantitatively compare the concentration of surface-active species, quasi in-situ EPR was performed. Four signal peaks with an intensity ratio of 1:2:2:1 were detected, which indicated the formation of DMPO-OH species (Fig. 4e). The DMPO-OH formed under negative potential might be attributed to the Forrester-Hepburn mechanism[39], where DMPO experienced nucleophilic addition by H₂O and coupled with an electron acceptor (Ni²⁺ → Ni⁰) (Supplementary Discussion 1, Supplementary Fig. S49). D-Ni(OH)₂/Ni@CF exhibited a stronger signal than Ni(OH)₂/Ni@CF, indicating superior surface water activation and a faster conversion rate from Ni²⁺ to Ni⁰ on D-Ni(OH)₂/Ni@CF. This was consistent with the conclusions reported by in-situ Raman results. Similar phenomena were also observed in the electrolyte without NO₃⁻ (Supplementary Fig. S36). Moreover, kinetic isotopic effect (KIE) was investigated to reveal H₂O dissociation rate by comparing the activities in H₂O and D₂O electrolytes. Although the NH₃ selectivity remained stable (Supplementary Fig. S37), the current density and NH₃ production rate declined significantly due to the sluggish D₂O dissociation. The calculated KIE value (KIE = k_H/k_D) was 1.87 for Ni(OH)₂/Ni@CF, while dropped to 1.37 over D-Ni(OH)₂/Ni@CF (Fig. 4f, g). The smaller KIE value reflected the accelerated water dissociation kinetic during NO₃RR, which validated the D-Ni(OH)₂/Ni@CF interface facilitated water activation, promoting the OH cycle together with OH adsorption and hydrogenation of N species[40].

Performance of NH₃ synthesis via NO₃RR

The NH₃ yield and selectivity of D-Ni(OH)₂/Ni@CF were systematically evaluated using UV spectrophotometer and nuclear magnetic resonance (NMR) (Supplementary Fig. S38). The difference in NH₃ production rate between the UV method and ion chromatography was within 5%, validating the accuracy of the measurements (Supplementary Figs. S39–41). D-Ni(OH)₂/Ni@CF exhibited enhanced NH₃ production activity at all potentials, achieving the maximal FE_{max} of 98.99%

(compared to 60.98% for Ni(OH)₂/Ni@CF) with a NH₃ production rate of 47.85 mg h⁻¹ cm⁻² (compared to 24.66 mg h⁻¹ cm⁻² for Ni(OH)₂/Ni@CF) at −0.8 V vs. RHE (Fig. 5a, b, and Supplementary Fig. S42). The activity of NH₃ production reflected the enhanced NO₃RR activity and kinetics attributed to the engineering of the dynamic interface by NTP. Furthermore, a range of Ni(OH)₂/Ni catalysts with varying proportions were synthesized to distinguish the impacts of OH cycle and electronic structure modulation (Supplementary Fig. S43, 44). The current density of the Ni(OH)₂/Ni heterogeneous structure demonstrated a volcano trend with the augmentation of the metallic Ni phase. The maximum current density of Ni(OH)₂/Ni₅:₅@CF approached −335.9 mA cm⁻², while was still lower than that of D-Ni(OH)₂/Ni@CF (−395.8 mA cm⁻²) (Supplementary Fig. S45). Furthermore, the FE of Ni(OH)₂/Ni heterogeneous structure (FE = 50–70%) was notably inferior to that of D-Ni(OH)₂/Ni@CF (FE = ~100%), corroborating that the superior catalytic performance of D-Ni(OH)₂/Ni@CF, which might be also originated from the defects and the enhanced OH cycle not only the effect of catalyst structure (Supplementary Fig. S46).

Subsequently, we examined the electrocatalytic performance of D-Ni(OH)₂/Ni@CF across a wide range of NO₃⁻ concentrations to simulate different industrial scenarios. The polarization curves displayed current density increased with NO₃⁻concentration (Supplementary Fig. S47). As expected, D-Ni(OH)₂/Ni@CF exhibited high FE (>99%) at 10,000 ppm, and still maintained considerable FE (>80%) at 2000 ppm with potential intense HER competition (Fig. 5c). Furthermore, consecutive 50 cycles of operation confirmed the stable NH₃ production rate and FE (Fig. 5d, and Supplementary Fig. S50). The valence state was relatively stable after reaction (Supplementary Fig. S48). D-Ni(OH)₂/Ni@CF exhibited an improvement of Ni-based catalysts for NO₃RR, indicating the potential for renewable energy-driven NH₃ synthesis (Table. S5). Techno-economic analysis (TEA) combined with sensitivity analysis was carried out to ascertain the economic potential (Supplementary Discussion 2). Under the current catalyst performance, the NH₃ production cost by NO₃RR was

calculated to be 1487 \$ t^{-1}. Given its sensitivity to the electricity price (Supplementary Fig. S51), the route of NH$_3$ synthesis through NO$_3$RR remains appealing with further improvements on renewable energy, thereby exhibiting promising application potential.

In summary, we adopted Ni(OH)$_2$ as model catalyst to investigate the mechanism of dynamic interface on NO$_3$RR. In-situ characterization and theoretical calculation revealed the potential-dependent change from Ni(OH)$_2$ to Ni(OH)$_2$/Ni, along with a local-OH-enrich region assumed to be formed at the dynamic interface. During NO$_3$RR, a potential interfacial OH cycle was established based on negative potential and microenvironment, related to the whole processes including de-hydroxylation, equilibrium of water dissociation and OH adsorption, etc. Furthermore, the dynamic surface was further activated to promote the OH cycle via surface vacancies pre-construction. As a result, D-Ni(OH)$_2$/Ni@CF exhibited excellent NO$_3$RR catalytic performance, achieving a high current density of NH$_3$ production and FE at a broad window of nitrate concentrations. The insights of the activated dynamic interface provided guidance for the rational design and optimization of highly efficient catalysts, to promote sustainable alternatives to harvest green NH$_3$ with renewable energy.

Methods
Electrocatalyst preparation
Commercial Cu foam (CF) (Sinero Technology, Suzhou) was utilized as the catalyst substrate. To remove surface oxides, CF was drenched with 3 M HCl (Sinopharm, AR) and then repeatedly rinsed with deionized water and ethanol (Sinopharm, AR), followed by sonication for 10 min to remove the surface HCl. Then, the substrate was dried in a vacuum environment at 50 °C for 1 h. The nanostructure Ni(OH)$_2$ material was synthesized by a facile electrodeposition strategy using a typical three-electrode system, with Ag/AgCl (GaossUnion) as the reference electrode, carbon rod (GaossUnion) as the counter electrode, and CF as the working electrode, respectively. Within 0.05 M H$_2$SO$_4$ (Sinopharm, AR) and 20 mM Ni(NO$_3$)$_2$ (Sinopharm, AR) electrolyte, cyclic voltammetry for 6 cycles (0.1 mV s^{-1}) in the range of −1 - 0.5 V vs. RHE was performed, followed by a constant potential of −1.1 V vs. Ag/AgCl for 600 s. The prepared electrocatalyst was repeatedly rinsed and dried before a typical test. Inductively coupled plasma (ICP) using Ar as carrier gas was employed to facilely construct vacancies on the nanostructure Ni(OH)$_2$@CF surface. Different injected power of ICP source (100 W, 200 W, and 300 W) was adjusted to investigate the effect of vacancy concentration, while the treated electrocatalysts were labeled as D$_{100}$-Ni(OH)$_2$@CF, D$_{200}$-Ni(OH)$_2$@CF, and D$_{300}$-Ni(OH)$_2$@CF, respectively. In this work, D$_{100}$-Ni(OH)$_2$@CF was mainly researched.

Materials characterizations
The microscopic morphology and microregion elemental composition of the electrocatalyst was characterized by the scanning electron microscope (SEM, ZEISS Sigma 300, SmartEDX). The nanostructure and lattice arrangement of the electrocatalyst were observed by a high-resolution transmission electron microscope (HRTEM, I Talos F200S). The crystal characterization and alignment destination of the electrocatalyst were verified by X-ray diffraction (XRD, Rigaku Ultima IV 3 kW, Cu Kα1). The chemical states and components of the electrocatalysts were detected by X-ray photoelectron spectroscopy (XPS, Thermo Scientific K-Alpha). The X-ray absorption fine structure spectra (XAFS) K-edge were collected at Shanghai Synchrotron Radiation Facility (SSRF), China. The positron annihilation lifetime spectroscopy (PALS) was measured via the apparatus DPLS3000. The lifetime of the positron could be calculated as followed[41–43]:

$$N(t) = \sum_i I_i / \tau_i \exp(-t/\tau_i) \tag{1}$$

Surface vacancy concentration was measured by electron paramagnetic resonance spectrometry (EPR, Bruker ESRA-300). The pH values of the electrolytes were measured by a pH meter (PHS-3E, Leici) (Supplementary Fig. S52). All 'a. u.' labels in this work referred to the arbitrary units.

In-situ experiments
In-situ Raman characterizations were performed to measure the chemical composition on a confocal Raman spectrometer (Raman, Renishaw InVia Reflex). The wavelength of the Raman excitation laser was selectively chosen as 633 nm. The silicon peak correction procedure was executed to assess the precision of the experiment. An in-situ Raman characterization was performed using a three-electrode system (Supplementary Fig. S53), wherein a Pt wire (GaossUnion) and an Ag/AgCl electrode filled with 3 M KCl served as the counter electrode and reference electrode, respectively, and the catalyst was employed as the working electrode. 1 M KOH (Sinopharm, AR) and 0.1 M KNO$_3$ (Sinopharm, AR) were utilized as the electrolyte. The potentiostatic electrolysis was carried out over a potential range from 0 to −0.9 V vs. RHE and for a duration of 30 minutes at a fixed potential of −0.8 V vs. RHE.

In-situ EPR measurements were employed to record the reaction behavior during electrochemical reactions (EPR, Bruker ESRA-300). The NO$_3$RR was conducted in a 10 ml H-cell with 1 M KOH + 0.1 M KNO$_3$ electrolyte, using a membrane for separation. A Pt plate, an Ag/AgCl electrode filled with 3 M KCl, and the catalyst served as the counter electrode, reference electrode, and working electrode, respectively. After 300 s of potentiostatic operation at −0.8 V vs. RHE, 0.5 mL of diluted DMPO was introduced into the electrolyte. Sample analysis was performed after thorough stirring for 100 s.

In-situ FTIR spectrums were obtained to determine the surface absorption species on catalyst surface (Thermo Fisher, Nicolet iS50) The catalyst was stripped from the CF and processed into an ink for deposition onto a glassy carbon electrode (GaossUnion), followed by drying to form the working electrode. In the three-electrode system, Pt wire and Ag/AgCl (3 M KCl) electrodes were utilized as the counter and reference electrodes, respectively. An electrochemical cell (30 ml) was utilized (Supplementary Fig. S53). FTIR data were recorded in reflection mode. Before data acquisition, the background of the working electrode was recorded in the open circuit potential. The working electrode was maintained at −0.8 V vs. RHE during NO$_3$RR.

In-situ DEMS measurements were conducted by using QAS100 instrument (Linglu China) to capture volatile intermediates and products. A catalyst-coated electrode, Pt wire, and Ag/AgCl electrode were employed as the working electrode, counter electrode, and reference electrode, respectively. An electrochemical cell (50 ml) was utilized (Supplementary Fig. S12). Volatile products were transported through a PTFE membrane via a vacuum pump to the mass spectrometer. The DEMS primarily targeted products with mass-to-charge ratios (m/z) of 17, 18, 19, and 20 (corresponding to NH$_3$, NH$_2$D, NHD$_2$, and ND$_3$, respectively). The DEMS test comprised two steps: firstly, the two groups of catalysts underwent NO$_3$RR in D$_2$O (Sinopharm, 99.8% D), and H$_2$O solvents, respectively. Subsequently, the catalysts were tested in H$_2$O solvent using LSV method for working cycle after thoroughly rinsed.

Electrochemical measurements
Electrochemical measurements were performed using an H-type electrolytic cell (GaossUnion, 50 ml) via the electrochemical workstation (CHI 760E), with the prepared catalyst as the working electrode (0.5 cm^2), an Ag/AgCl electrode (filled with 3 M KCl) as the reference electrode, and a Pt foil (GaossUnion) as the counter electrode, respectively. 1 M KOH mixed with different KNO$_3$ concentration was used as the cathodic electrolyte (mostly 0.1 M KNO$_3$) and 0.5 M H$_2$SO$_4$ was used as the anodic electrolyte, respectively, which was separated by a bipolar membrane (Fumatech, FBM-PK, 130–150 μm)[44]. The

electrolyte was preserved at room temperature and was deoxygenated by Ar-purging before testing. To avoid environmental interference, the cathodic chamber was first bubbled with Ar gas for 15 min at a flow rate of 30 sccm, which was controlled by a mass flow meter. Then Ar was kept purged during the electrochemical test. Linear sweep voltammetry (LSV) test was performed with the scan rate of 5 mV s^{-1}. Electrochemical impedance was performed at the open-circuit potential with the frequency of 0.01 Hz to 100 kHz. To evaluate the electrochemical active surface area, cyclic voltammetry was performed by scanning in the non-Faraday region with the rate of 20, 40, 60, 80, and 100 mV s^{-1}. All the potentials reported were calibrated to the reversible hydrogen electrode (RHE) reference scale using:

$$E(V \text{ vs. RHE}) = E(V \text{ vs. Ag/AgCl}) + 0.0591 \times pH + 0.21 \quad (2)$$

The equation was calibrated by hydrogen reversible reaction (Supplementary Fig. S54). All data were reported without iR compensation, the resistance between RE and WE were also reported (Supplementary Fig. S55). Constant potential experiments were performed at −0 V, −0.2 V, −0.4 V, −0.6 V, −0.8 V, and −1.0 V vs. RHE at a constant potential with a stirring speed of 500 rpm for 1 h. All the experiments were repeated to ensure accuracy.

Calculation of NH₃ yield rate and FE

The concentration of synthesized NH₃ was quantitatively assessed via the Indophenol blue method[45]. The electrolyte was first diluted to within the detectable range. 4 ml diluted electrolyte was then combined with 2.4 ml of Reagent A, 0.8 ml of Reagent B, and 0.32 ml of Reagent C. Reagent A: 100 ml solution of 6.40 g $C_7H_5O_3Na$ (Aladdin, AR) + 1.31 g NaOH (Macklin, AR) in deionized H_2O; Reagent B: 100 ml solution of 3.08 g NaOH + 7.5 ml NaClO (Aladdin, AR) in deionized H_2O; Reagent C: 100 ml solution of 1 g $C_5FeN_6Na_2O$ (Aladdin, AR) in 100 ml H_2O. After two hours, the absorption spectrum was measured via the UV-visible spectrophotometer (UV-3100), and the NH₃ concentration was determined based on the absorbance at 655 nm. Calibration curves correlating concentration and absorbance were created with a standard NH₄Cl solution. To verify the accuracy of the Indophenol blue method, ion chromatography (IC) was also employed. By determining the NH₃ concentration, the production rate of NH₃ was calculated as below:

$$\text{NH}_3 \text{ Production rate} = \frac{c_{NH_3} V}{A_{cat} t} \quad (3)$$

where c_{NH_3} represented the NH₃ concentration; V represented the volume of the electrolyte (50 ml); A_{cat} represented the area of the catalyst (0.5 cm^2); t represented the operating time. The Faradaic efficiency (FE) of NH₃ was calculated as below:

$$\text{FE}_{NH3} = \frac{n c_{NH_3} F V}{it} \quad (4)$$

where n represented the electron transfers number of 8 in NO₃RR, F represented the Faraday constant of 96,485 C mol^{-1}, and i represented the current density (mA cm^{-2}).
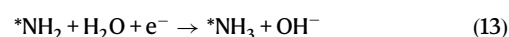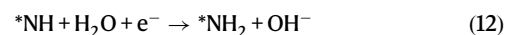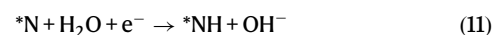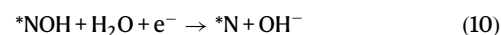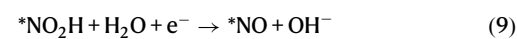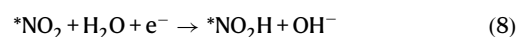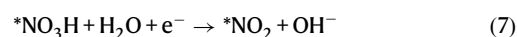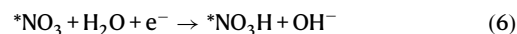
Isotope tracing measurement

The electrolyte was resolved using Nuclear Magnetic Resonance (NMR, Brucke 0707166Q 600 MHz). ^1H NMR spectroscopy was used to trace the nitrogen source of generated NH₃. ^{15}N labelled nitrate was electrocatalytically reduced reaction, while the electrolyte was collected and diluted to the measurement range. Hydrochloric acid was added to adjust the pH to 2.0. Next, 0.5 ml of sample solution was mixed with 0.05 D₂O ml, and $C_4H_4O_4$ (Sigma-Aldrich, AR) was used as an internal standard.

DFT calculations

All DFT calculations in this work were performed by using the Vienna ab initio simulation program (VASP)[46]. The projector-augmented plane-wave (PAW) method was employed to characterize the ion-electron interactions[47]. The generalized gradient approximation (GGA), as formulated by Perdew-Burke-Ernzerhof (PBE), was utilized with an energy cutoff of 450 eV[48]. Inverse space was sampled using the Monkhorst-Pack method, with a 3 × 3 × 1 k-point grid in the Brillouin zone. The convergence criteria were set to 10^{-5} eV for energy and 0.02 eV Å^{-1} for the Hellmann-Feynman forces on each atom. The DFT + U method was implemented with a parameter value of 6.2 eV for Ni[49]. To prevent interactions between adjacent layers, a vacuum layer was introduced. Additionally, the crystal orbital Hamilton population (COHP) was generated using the Lobster to illustrate the contributions of bonding and antibonding interaction[50]. The Gibbs free energy (ΔG) was defined as:

$$\Delta G = \Delta E + \Delta ZPE - T\Delta S \quad (5)$$

where ΔE represented the total energy, ΔZPE represented the zero-point energy, T represented the temperature, and ΔS represented entropy, respectively. The NO₃RR was calculated according to the following reactions[51]:

$$*NO_3 + H_2O + e^- \rightarrow *NO_3H + OH^- \quad (6)$$

$$*NO_3H + H_2O + e^- \rightarrow *NO_2 + OH^- \quad (7)$$

$$*NO_2 + H_2O + e^- \rightarrow *NO_2H + OH^- \quad (8)$$

$$*NO_2H + H_2O + e^- \rightarrow *NO + OH^- \quad (9)$$

$$*NOH + H_2O + e^- \rightarrow *N + OH^- \quad (10)$$

$$*N + H_2O + e^- \rightarrow *NH + OH^- \quad (11)$$

$$*NH + H_2O + e^- \rightarrow *NH_2 + OH^- \quad (12)$$

$$*NH_2 + H_2O + e^- \rightarrow *NH_3 + OH^- \quad (13)$$

Where the * represents the adsorption site.

Data availability

The experiment data generated in this study are provided with this paper in the Supplementary Information and Source Data file. Source data are provided in this paper.

References

1. Soloveichik, G. Electrochemical synthesis of ammonia as a potential alternative to the Haber-Bosch process. *Nat. Catal.* **2**, 377–380 (2019).
2. Kyriakou, V., Garagounis, I., Vourros, A., Vasileiou, E. & Stoukides, M. An electrochemical haber-bosch process. *Joule* **4**, 142–158 (2020).
3. Zi, X. et al. Vacancy-rich 1T-MoS2 monolayer confined to MoO3 matrix: an interface-engineered hybrid for efficiently electrocatalytic conversion of nitrogen to ammonia. *Appl. Catal. B Environ.* **286**, 119870 (2021).
4. Kitano, M. et al. Ammonia synthesis using a stable electride as an electron donor and reversible hydrogen store. *Nat. Chem.* **4**, 934–940 (2012).

5. Wang, Q., Guo, J. & Chen, P. Recent progress towards mild-condition ammonia synthesis. *J. Energy Chem.* **36**, 25–36 (2019).

6. Zhao, C. et al. Ambient electrosynthesis of ammonia on a biomass-derived nitrogen-doped porous carbon electrocatalyst: contribution of pyridinic nitrogen. *ACS Energy Lett.* **4**, 377–383 (2019).

7. Erisman, J. W., Sutton, M. A., Galloway, J., Klimont, Z. & Winiwarter, W. How a century of ammonia synthesis changed the world. *Nat. Geosci.* **1**, 636–639 (2008).

8. Chen, J. G. et al. Beyond fossil fuel-driven nitrogen transformations. *Science* **360**, eaar6611 (2018).

9. Xu, X. et al. 1T-phase molybdenum sulfide nanodots enable efficient electrocatalytic nitrogen fixation under ambient conditions. *Appl. Catal. B Environ.* **272**, 118984 (2020).

10. Yang, X. et al. Molecular single iron site catalysts for electrochemical nitrogen fixation under ambient conditions. *Appl. Catal. B Environ.* **285**, 119794 (2021).

11. Montoya, J. H., Tsai, C., Vojvodic, A. & Nørskov, J. K. The challenge of electrochemical ammonia synthesis: a new perspective on the role of nitrogen scaling relations. *ChemSusChem* **8**, 2180–2186 (2015).

12. Wu, A. et al. Direct ammonia synthesis from the air via gliding arc plasma integrated with single atom electrocatalysis. *Appl. Catal. B Environ.* **299**, 120667 (2021).

13. Wang, C. et al. Modulating CoFe2O4 nanocube with oxygen vacancy and carbon wrapper towards enhanced electrocatalytic nitrogen reduction to ammonia. *Appl. Catal. B Environ.* **297**, 120452 (2021).

14. Lai, F. et al. N2 electroreduction to NH3 by selenium vacancy-rich ReSe2 catalysis at an abrupt interface. *Angew. Chem. Int. Ed.* **59**, 13320–13327 (2020).

15. Tang, C. & Qiao, S. How to explore ambient electrocatalytic nitrogen reduction reliably and insightfully. *Chem. Soc. Rev.* **3**, 3166–3180 (2019).

16. Andersen, S. Z. et al. A rigorous electrochemical ammonia synthesis protocol with quantitative isotope measurements. *Nature* **570**, 504–508 (2019).

17. Zhang, L. et al. High-performance electrochemical NO reduction into NH3 by MoS2 nanosheet. *Angew. Chem. Int. Ed.* **60**, 25263–25268 (2021).

18. Wang, Y. et al. Enhanced nitrate-to-ammonia activity on copper-nickel alloys via tuning of intermediate adsorption. *J. Am. Chem. Soc.* **142**, 5702–5708 (2020).

19. Yang, M., Raucci, U. & Parrinello, M. Reactant-induced dynamics of lithium imide surfaces during the ammonia decomposition process. *Nat. Catal.* **6**, 829–836 (2023).

20. Rosca, V., Duca, M., Groot, M. T. & Koper, M. T. Nitrogen cycle electrocatalysis. *Chem. Rev.* **109**, 2209–2244 (2009).

21. Wang, Y., Zhou, W., Jia, R., Yu, Y. & Zhang, B. Unveiling the activity origin of a copper-based electrocatalyst for selective nitrate reduction to ammonia. *Angew. Chem. Int. Ed.* **59**, 5350–5354 (2020).

22. Fu, X. et al. Alternative route for electrochemical ammonia synthesis by reduction of nitrate on copper nanosheets. *Appl. Mater. Today* **19**, 100620 (2020).

23. Wang, Y., Wang, C., Li, M., Yu, Y. & Zhang, B. Nitrate electroreduction: mechanism insight, in situ characterization, performance evaluation, and challenges. *Chem. Soc. Rev.* **50**, 6720–6733 (2021).

24. Han, S. et al. Ultralow overpotential nitrate reduction to ammonia via a three-step relay mechanism. *Nat. Catal.* **6**, 402–414 (2023).

25. Ziegler, L. D. & Hudson, B. Resonance rovibronic Raman scattering of ammonia. *J. Phys. Chem.* **88**, 1110–1116 (1984).

26. Desilvestro, J., Corrigan, D. A. & Weaver, M. J. Spectro-electrochemistry of thin nickel hydroxide films on gold using surface-enhanced Raman spectroscopy. *J. Phys. Chem.* **90**, 6408–6411 (1986).

27. Koops, T., Visser, T. & Smit, W. M. A. Measurement and interpretation of the absolute infrared intensities of NH3 and ND3. *J. Mol. Struct.* **96**, 203–218 (1983).

28. Lin, C. et al. *Nat. Catal.* **4**, 1012–1023 (2021).

29. Tan, X. et al. Electrochemical etching switches electrocatalytic oxygen evolution pathway of IrOx/Y2O3 from adsorbate evolution mechanism to lattice-oxygen-mediated mechanism. *Small* **19**, 2303249 (2023).

30. Chen, X. et al. Promoting water dissociation for efficient solar driven CO₂ electroreduction via improving hydroxyl adsorption. *Nat. Commun.* **14**, 751 (2023).

31. Zhang, T. et al. Engineering oxygen vacancy on NiO nanorod arrays for alkaline hydrogen evolution. *Nano Energy* **43**, 103–109 (2018).

32. Cui, J., Tan, J., Zhu, Y. & Cheng, F. Aqueous hydrogenation of levulinic acid to 1,4-pentanediol over Mo-modified Ru/activated carbon catalyst. *ChemSusChem* **11**, 1316 (2018).

33. Vanhaelst, M. & Clauws, P. EPR spectrum of the oxygen vacancy in single crystals V2O5. *Phys. Solid State* **87**, 719–723 (1978).

34. Li, S. et al. Oxygen-evolving catalytic atoms on metal carbides. *Nat. Mater.* **20**, 1240–1247 (2021).

35. Uhlenbrock, S., Scharfschwerdt, C., Neumann, M., Illing, G. & Freund, H. The influence of defects on the Ni 2*p* and O 1*s* XPS of NiO. *J. Phys. -Condens Mat.* **4**, 7973–7978 (1992).

36. Zhang, N. et al. Surface activation and Ni-S stabilization in NiO/NiS2 for efficient oxygen evolution reaction. *Angew. Chem. Int. Ed.* **61**, e202207217 (2022).

37. Zhan, B. et al. Defect-induced triple synergistic modulation in copper for superior electrochemical ammonia production across broad nitrate concentrations. *Nat. Commun.* **15**, 2816 (2024).

38. Liao, W. et al. Sustainable conversion of alkaline nitrate to ammonia at activities greater than 2 A cm⁻². *Nat. Commun.* **15**, 1264 (2024).

39. Forrester, A. R. & Hepburn, S. P. Spin traps. A cautionary note. *J. Chem. Soc. C,* 701–703 https://doi.org/10.1039/J39710000701 (1971).

40. Gennero de Chialvo, M. R. & Chialvo, A. C. Existence of two sets of kinetic parameters in the correlation of the hydrogen electrode reaction. *J. Electrochem. Soc.* **147**, 1619 (2000).

41. Tuomisto, F. & Makkonen, I. Defect identification in semiconductors with positron annihilation: experiment and theory. *Rev. Mod. Phys.* **85**, 1583 (2013).

42. Guan, M. et al. Vacancy associates promoting solar-driven photocatalytic activity of ultrathin bismuth oxychloride nanosheets. *J. Am. Chem. Soc.* **135**, 10411–10417 (2013).

43. Zhu, K. et al. Defect engineering on V2O3 cathode for long-cycling aqueous zinc metal batteries. *Nat. Common.* **12**, 6878 (2021).

44. Wu, A. et al. Electrocatalytic Disproportionation of Nitric Oxide Toward Efficient Nitrogen Fixation. *Abstract Advanced Energy Materials* **13**, 2204231 (2023).

45. Horn, D. B. & Squire, C. R. The estimation of ammonia using the indophenol blue reaction. *Clin. Chim. Acta* **14**, 185–194 (1966).

46. Kresse, G. & Furthmüller, J. Efficiency of ab-initio total energy calculations for metals and semiconductors using a plane-wave basis set. *Comput. Mater. Sci.* **6**, 15–50 (1996).

47. Blöchl, P. E. Projector augmented-wave method. *Phys. Rev. B.* **50**, 17953 (1994).

48. Perdew, J. P., Burke, K. & Ernzerhof, M. Generalized gradient approximation made simple. *Phys. Rev. Lett.* **7**, 3865–3868 (1996).

49. Cai, T. et al. Study on the ground state of NiO: the LSDA (GGA)+U method. *Phys. Rev. B Condens* **404**, 89–94 (2009).

50. Nelson, R. et al. LOBSTER: local orbital projections, atomic charges, and chemical-bonding analysis from projector-augmented-wave-based density-functional theory. *J. Comput Chem.* **41**, 1931–1940 (2020).

51. Zhu, X. et al. Mott-Schottky contact synergistically boosts the electroreduction of nitrate to ammonia under low-nitrate concentration. *Energy Environ. Sci.* **17**, 2908–2920 (2024).

Author contributions

A.W. and H.-B.W. conceived the idea and designed the experiments. A.W., X.L., and J.Y. supervised the project. J.L. carried out the experiments. J.L., Y.Z., and A.C. performed the calculations. A.W., Q.L., and J.L. wrote the paper. All authors discussed the results and commented on the paper.

Competing interests

The authors declare no competing interests.

Additional information

Supplementary information The online version contains supplementary material available at https://doi.org/10.1038/s41467-024-50988-5.

Correspondence and requests for materials should be addressed to Hao Bin Wu, Jianhua Yan or Angjian Wu.

Peer review information *Nature Communications* thanks Yijin Kang, Dongdong Zhu and the other anonymous reviewer(s) for their contribution to the peer review of this work. A peer review file is available.

Reprints and permissions information is available at http://www.nature.com/reprints

Publisher's note Springer Nature remains neutral with regard to jurisdictional claims in published maps and institutional affiliations.